Chemical Science

ROYAL SOCIETY OF CHEMISTRY

EDGE ARTICLE

View Article Online
View Journal | View Issue

Cite this: *Chem. Sci.*, 2023, **14**, 3286

All publication charges for this article have been paid for by the Royal Society of Chemistry

Received 13th November 2022
Accepted 20th February 2023

DOI: 10.1039/d2sc06244e

rsc.li/chemical-science

BINOL-like atropisomeric chiral nanographene†

Shengtao Li,[a] Ranran Li,[a] Yi-Kang Zhang,[a] Shutao Wang,[b] Bin Ma,[a] Bin Zhang[a] and Peng An *[a]

Interest in making chiral polycyclic aromatic hydrocarbons (PAHs) or nanographenes (NGs) has greatly increased recently. To date, a majority of chiral nanocarbons have been designed based on helical chirality. Here, we describe a novel atropisomeric chiral oxa-NG **1** by the selective dimerization of naphthalene-containing, hexa-*peri*-hexabenzocoronene (HBC)-based PAH **6**. The photophysical properties of the oxa-NG **1** and monomer **6** were investigated, including UV-vis absorption (λ_{max} = 358 nm for **1** and **6**), fluorescence emission (λ_{em} = 475 nm for **1** and **6**), fluorescence decay (15 *vs.* 16 ns), and fluorescence quantum yield, and it was found that the photophysical properties of the monomer are nearly maintained in the NG dimer due to its perpendicular conformation. Single-crystal X-ray diffraction analysis shows that both enantiomers cocrystallize in a single crystal, and the racemic mixture can be resolved by chiral high-performance liquid chromatography (HPLC). The circular dichroism (CD) spectra and circularly polarized luminescence (CPL) of the enantiomers of **1**-*S* and **1**-*R* were studied and the CD and CPL spectra exhibited opposite Cotton effects and fluorescence signals. Density functional theory (DFT) calculations and HPLC-based thermal isomerization results showed that the racemic barrier is as high as 35 kcal mol^{-1}, suggesting a rigid chiral nanographene structure. Meanwhile, *in vitro* studies indicated that oxa-NG **1** is an efficient photosensitizer for white-light-induced singlet oxygen generation.

Introduction

Due to their attractive three-dimensional structures, intriguing optoelectronic properties, and broad applications in organic electronics, contorted polycyclic aromatic hydrocarbons (PAHs or nanographenes, NGs) have received considerable attention in recent decades.[1] In particular, the introduction of chirality in the synthesis of contorted PAHs or NGs by a bottom-up approach leads to interesting chiral hydrocarbons and tunable chiroptical nanomaterials.[2] Among these chiral NGs, helicenes represent the dominant class of compounds by virtue of their inherent helical chirality.[3] Strategically, the inherent helicity can be constructed by the introduction of crowdedness by bulky substituents in the bay, cove, or fjord regions in the PAHs or NGs[4] or strain-induced curvature by the incorporation of non-hexagonal rings or helical units.[5]

As a conventional NG unit, hexa-*peri*-hexabenzocoronene (HBC) and its derivatives have continuously been intensively researched.[6] Recently, HBC-based helical chiral NGs have been developed by using the aforementioned strategy in their "monomer"[5b,7] or π-extended forms.[8] For example, several chiral "HBC-dimers" with helical conformations have been synthesized. As shown in Fig. 1a, by embedding an oxa[7]helicene unit as a linker, Jux *et al.* reported a helical "HBC-dimer" as a circularly polarized luminescence chromophore.[9] Martín *et al.* constructed chiral bilayer nanographene with a [10]helicene unit fused in an "HBC-dimer" (Fig. 1a).[10] Campaña *et al.* and Wang *et al.* reported helical HBC dimers with single or pairs of [5]helicene (Fig. 1a), substituted with *tert*-butyl groups at the two ends of the fjord region.[8b,11] In addition to the introduction of nonhexagonal rings, Feng and Liu's groups reported HBC-based helical nanographenes containing an azulene-embedded helicene.[12] In addition to helicity, axial chirality which refers to the chiral molecules that contain a chirality axis – an axis about which a set of groups is arranged so that the spatial arrangement is not superimposable on its mirror image is less utilized in the construction of chiral NGs. As the only example to date, Martín *et al.* recently reported a helical arrangement, chiral nanographene bearing a chiral axis along the whole molecule.[13] Their helical arrangement stems from a chiral axis.

As the best-known representative of axially chiral molecules, enantiomeric atropisomers of 1,1′-binaphthyl-2,2′-diol (BINOL) (Fig. 1) as chiral auxiliaries have been extensively investigated in asymmetric synthesis and enantioselective fluorescence sensors.[14] Due to their accessibility and relatively high rotational barriers, some BINOL derivatives with extended

[a]*School of Chemical Science and Technology & Key Laboratory of Medicinal Chemistry for Natural Resource, Ministry of Education, Yunnan University, Kunming 650091, P. R. China. E-mail: anp@ynu.edu.cn*

[b]*College of Chemistry and Chemical Engineering, Lanzhou University, Lanzhou 730000, P. R. China*

† Electronic supplementary information (ESI) available. CCDC 2193890. For ESI and crystallographic data in CIF or other electronic format see DOI: https://doi.org/10.1039/d2sc06244e

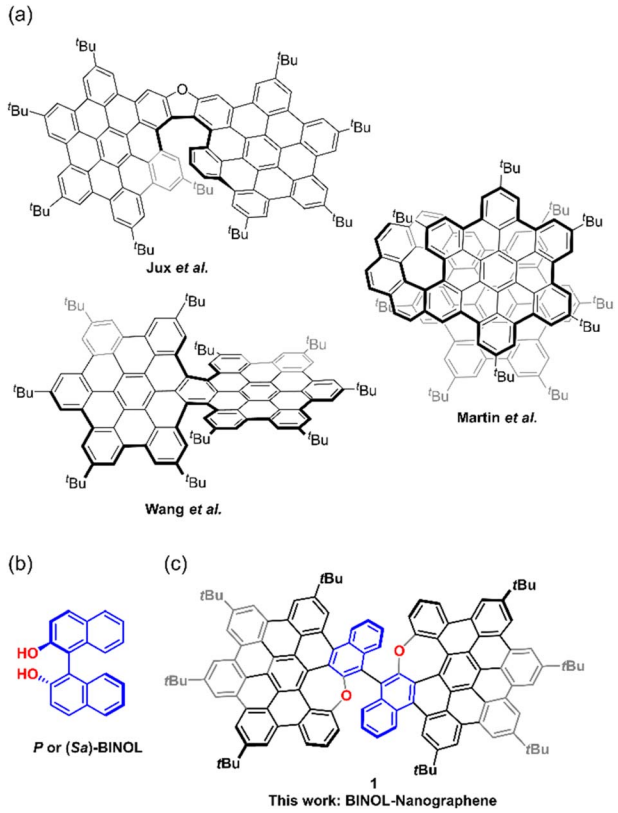

Fig. 1 (a) Representative structures of helical "HBC-dimer". (b) Structure of *S*-atropisomer of BINOL, with nomenclature of S_a (subscript indicating an axial chirality). (c) BINOL-like oxa-nanographene **1** (only the *S*-form enantiomer of **1** is shown).

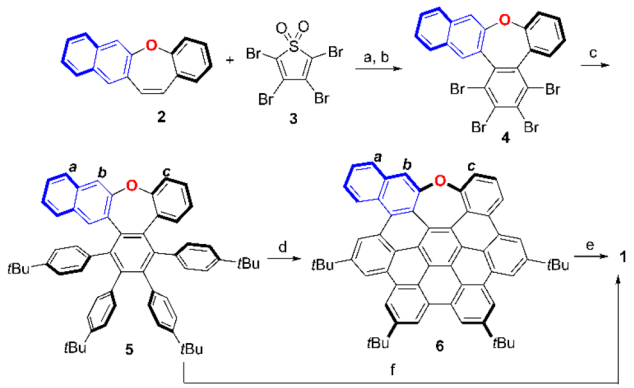

Scheme 1 Synthetic route to oxa-nanographenes **1** and **6**. Reagents and conditions: (a) toluene, 110–120 °C, 20 h. (b) DDQ (2.0 equiv.), DCM, toluene, rt, 30 min, yield 81%. (c) 4-*tert*-butylphenylboronic acid, $Pd(CH_3CN)_2Cl_2$ (20%), SPhos (40%), K_3PO_4, Xylene, 150 °C, 72 h, yield 85%. (d) DDQ (5.0 equiv.), CF_3SO_3H (13.0 equiv.), DCM, 0 °C, yield 64%. (e) DDQ (2.0 equiv.), CF_3SO_3H (6.0 equiv.), DCM, 0 °C, yield 55%. (f) DDQ (6.0 equiv.), CF_3SO_3H (33.0 equiv.), DCM, 0 °C, yield 60%.

conjugation have been prepared[15] and the enantiomeric BINOL derivatives, which also served as chiral inducers or transfer scaffolds, were introduced into the hydrocarbons to create diverse chiral materials.[16–18] For instance, by the introduction of chiral binaphthyl scaffolds, different chiral carbon nanorings or macrocycles were prepared as circularly polarized luminescence (CPL) emitters.[16] Quite recently, Würthner *et al.* reported a helical perylene bisimide (PBI) by combining an axially chiral binaphthol bisimide (BBI), in which the BBI serves as a chirality transfer unit to generate helical twisted PBI.[17] The Melle-Franco and Mateo-Alonso groups also created chiral molecular graphene nanoribbons by adding enantiomerically pure 1,1′-binaphthyl-2,2′-diamine (BINAM) precursors at both ends of the nanoribbons, and the axial chirality of BINAM was transferred to the aromatic framework to generate a helical conformer.[18]

Herein, we report a novel BINOL-like chiral oxa-nanographene **1** with a "BINOL" core fused to a "HBC-dimer" by selective dimerization of the oxygen-doped HBC units (Fig. 1b and c).

It is an unprecedented atropisomeric chiral nanographene with chirality stemming from an axially chiral "BINOL". Compared to HBC, the introduction of oxygen electronically activates the dimerization of the oxygen-doped monomer to form the HBC-dimer. Single-crystal X-ray analysis unequivocally reveals a pair of atropisomers in the racemic structures. The photophysical and chiroptical properties, including UV-vis, fluorescence spectra, circular dichroism (CD), and circularly polarized luminescence (CPL), were well investigated. Computational calculation and HPLC-based thermal isomerization results suggest that the racemization barrier of oxa-NG **1** is much higher than that of 1,1-binaphthyl, and comparable to that of BINOL, which gives a rigid chiral oxa-nanographene structure.

Results and discussion

Synthesis of oxa-nanographene 1

The synthetic route for oxygen-embedded NG **1** is depicted in Scheme 1 (for synthetic details refer to Scheme S1†). In brief, benzo[*b*]naphtho[2,3-*f*]oxepine **2** containing naphthalene was synthesized as a monomer of binaphthyl. The Diels–Alder reaction of structure **2** with tetrabromothiophene-*S*,*S*-dioxide **3** in toluene followed by oxidative aromatization in the presence of 2,3-dichloro-5,6-dicyano-1,4-benzoquinone (DDQ) afforded tetrabrominated aromatics **4** in 81% yield. Subsequently, a fourfold Suzuki–Miyaura cross-coupling of polybrominated compound **5** was performed in the presence of 20 mol% $PdCl_2(CH_3CN)_2$, 40 mol% SPhos, excess boronic acid, and K_3PO_4, affording hexaphenylbenzene **5** in 85% yield. Then, the Scholl-type cyclodehydrogenation of compound **5** was carried out in DDQ/CF_3SO_3H in DCM. When **5** equiv. of DDQ was added at 0 °C, the five-fold cyclization product **6** was obtained within 1 min in a 64% yield. The final step was the dimerization of compound **6** by reaction with dichlorodicyano-*p*-benzoquinone (DDQ) in the presence of triflic acid at 0 °C, which provided dimer **1** in 55% yield. Notably, only an aryl–aryl single bond at the *b* position was formed due to the electron donation of oxygen at the electron-rich naphthalene ring. Typical oxidative coupling conditions of 2-naphthol for BINOL synthesis such as $FeCl_3$ (ref. 19) or $CuSO_4/Al_2O_3$ (ref. 20) were not feasible for the synthesize of NG **1** by dimerization of the naphthalene

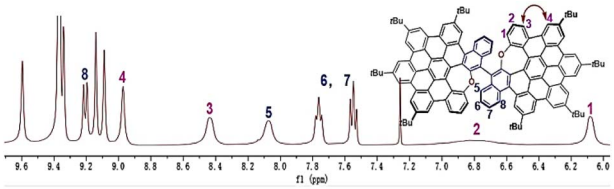

Fig. 2 Partial ^{1}H NMR spectrum ($CDCl_3$, 22 °C) and the structure with assigned protons (proton 1–8) of NG **1**. The red and blue numbers suggest two spin–spin coupling systems. Representative NOEs are depicted by red arrows.

derivative **6**. To our delight, by increasing the reagents, prolonging the reaction time, and enhancing the reaction concentration, dimer **1** could be obtained directly from compound **5** in 60% yield in one step.

Due to the crossed conformation of the aromatics at the end of the aryl–aryl single bond, oxa-NG **1** shows good solubility in common organic solvents such as DCM, chloroform, ethyl acetate, and benzene. Hence, structure **1** was unequivocally characterized by ^{1}H NMR, ^{13}C NMR, and 2D-NMR spectroscopy and HRMS (Fig. S12–S14†). In high-resolution matrix-assisted laser desorption/ionization-time-of-flight mass spectrometry (MALDI-TOF MS), structure **1** displayed a strong signal at m/z = 1622.7792, with isotopic distribution patterns consistent with the calculated spectrum (Fig. S15†). The ^{1}H NMR spectrum of dimer **1** indicates that the two monomer units showed identical signals with each other in the dimeric structure **1** (Fig. 2). The two groups of spin–spin coupling protons 1–3 and 5–8 were unequivocally confirmed by 2D ^{1}H–^{1}H COSY and ROESY (Fig. S13 and S14†). A nuclear Overhauser effect (NOE) between protons 3 and 4 was observed in the ^{1}H–^{1}H ROESY spectrum (Fig. S14†). Collectively, protons 1–8 are assigned in Fig. 2. Notably, the chemical shifts of the protons in the O-connected benzene ring were shifted upfield to approximately 6.5 ppm for proton 2 and 6.1 ppm for proton 1 due to the electron-donating resonance effect of oxygen and the shielding effect induced by spatial overlap with adjacent aromatic rings. Interestingly, structure **1** showed signal broadening for some protons in the axial single bond area (for example, protons 1, 2, 3, and 5). This phenomenon was presumably attributable to the restricted rotation of the axial aryl–aryl single bond of binaphthyl.

Crystallographic analysis of *rac*-1

Single crystals of oxa-nanographene **1** suitable for X-ray analysis were obtained by recrystallization from dichloromethane/ethyl acetate mixed solvents (Table S1†). The X-ray crystallographic analysis, shown in Fig. 3, revealed an "HBC-dimer", chiral construction in which two oxygen-doped HBC derivatives were connected through an axial aryl–aryl single bond (C18–C18′). *rac*-**1** crystallizes in the *C*12/*c*1 space group as a 1 : 1 racemic mixture. The **1**-*R* and **1**-*S* enantiomers display a complete mirror symmetry with BINOL-like axial chirality (Fig. 3a). The two naphthalene-containing aromatics are almost vertical with an 88° torsional angle between the naphthalenes (C19–C18–C18′–

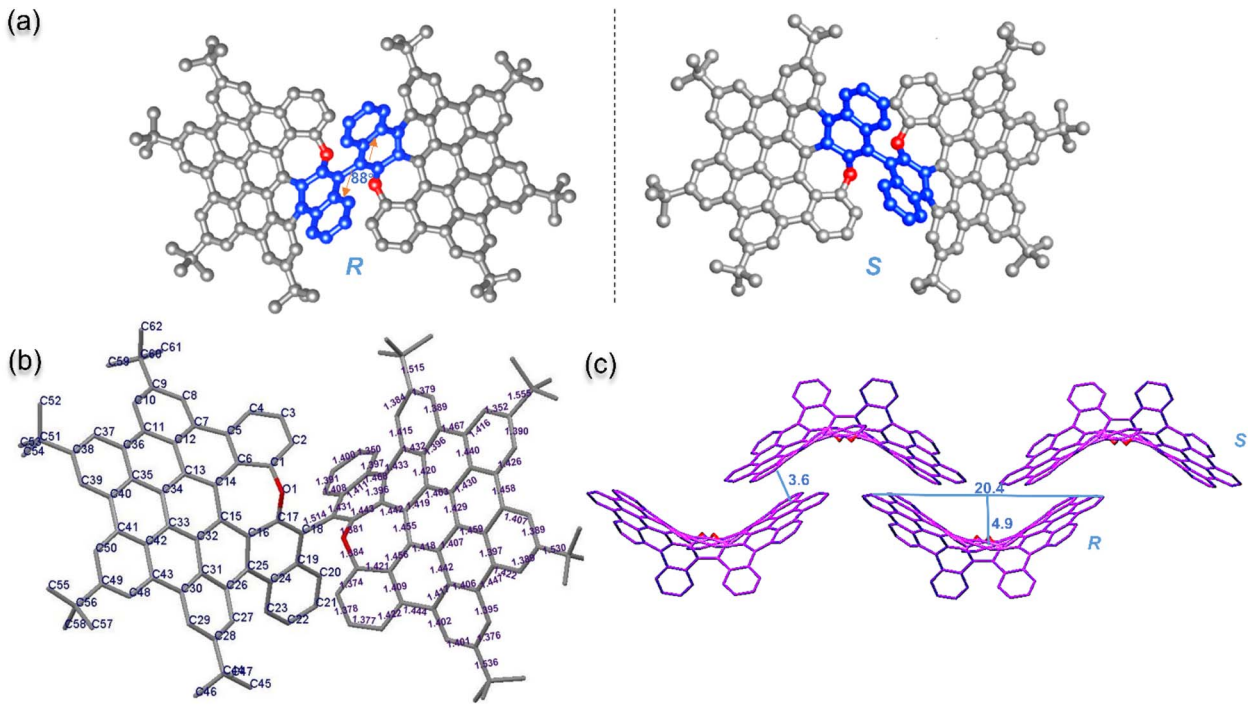

Fig. 3 X-ray crystallographic molecular structure of NG **1** with a 50% thermal ellipsoid probability.[21] Hydrogen atoms are omitted for clarity. (a) ORTEP drawing of the asymmetric atropisomers of oxa-NG **1**. The binaphthyl unit is highlighted in blue and the oxygen is highlighted in red in both the *R* and *S* enantiomers. (b) Backbone of oxa-NG **1** with carbons and bond lengths marked. (c) Molecular packing of racemic oxa-NG **1**; the top layer is the *S* conformation and the bottom layer is the *R* conformation.

C19′) in structure **1**, which is 9° larger than that of the original BINOL (79.2° torsional angle).[22] The aryl–aryl single bond is 1.514 Å, 0.02 Å longer than BINOL (1.494 Å bond length). The larger torsional angle and prolonged single-bond indicate the higher degree of torsion of structure **1** than that of BINOL. Due to embedding an oxepine seven-membered ring, each monomer of the O-doped HBC derivative displays a distorted saddle conformation (Fig. 3b) and structure **1** itself also forms a great saddle shape (Fig. 3c). The length of the saddle, defined as the distance between carbons C38 and C38′, is approximately 2 nm; thus, the depth of the saddle is approximately 0.5 nm. rac-**1** is stacked in an alternating manner to form pairs of enantiomers through π–π interactions with a π–π distance of 3.6 Å between each enantiomer (Fig. 3c and S1†).

Determination of the racemization barrier

With the confirmation of the atropisomers in the X-ray analysis, we evaluated the *S*/*R* racemization barrier of oxa-NG **1**. Density functional theory (DFT) calculations with the relative Gibbs free energy at the M06-2X/6-31G** level were performed to identify the transition state. A plausible isomerization pathway between the two enantiomers was proposed to proceed through a transition state with the two oxygen atoms and naphthalene rings in the *syn* conformation and the torsional angle for the binaphthyl scaffold decreasing to approximately 3° (Fig. 4 and S19†).

Accordingly, the *S*/*R* isomerization barrier was determined to be 37.0 kcal mol^{-1}.

Due to the high isomerization barrier, both enantiomers of compound **1** could be completely resolved and purified by chiral high-performance liquid chromatography (HPLC). To experientially determine the isomerization barrier, thermal racemization of optically pure **1**-*R* was performed followed by chiral HPLC analysis (Fig. S3†). HPLC traces of the samples after heating in 1,2-dichlorobenzene at 170 °C exhibited a clean transformation from the **1**-*R* to the **1**-*S* isomer, suggesting high thermal stability. The half-life ($\tau_{1/2}$) for the loss of enantiomeric excess was determined as 4 h at 170 °C. This gives a $\Delta G^{\ddagger}$ (443 K) of 35 kcal mol^{-1} using the Eyring equation, which is consistent with the computational result. This isomerization barrier is much higher than that of 1,1-binaphthyl, and comparable to that of BINOL,[14,23] indicating a high degree of optical stability of the pure enantiomers and the π-extension barely affected the atropisomerism of the binaphthyl framework.

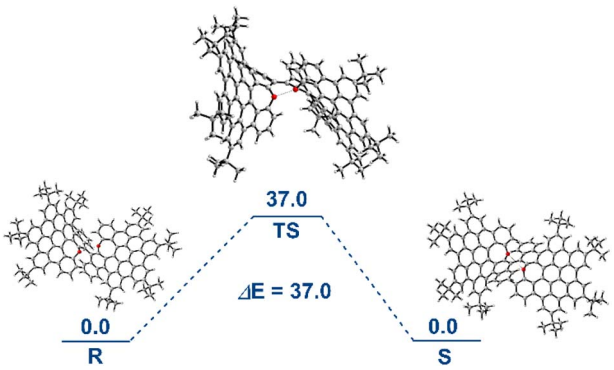

Fig. 4 Activation barrier for the isomerization process between *S* and *R* in units of kcal mol^{-1} at the M06-2X/6-31G** level of theory.

Photophysical and chiroptical properties

The photophysical and chiroptical properties were investigated for racemic oxa-NG **1** and each optically pure enantiomer. As shown in Fig. 5a, the absorption maxima of compound **1** appeared at 360 nm (ε = 1.7 × 105 M^{-1} cm^{-1}) with multiple shoulder peaks at 283 nm, 329 nm, 342 nm, 373 nm, 406 nm, and 427 nm. This low-energy band is mainly dominated by HOMO → LUMO + 1 and HOMO → LUMO at 367.4 nm (Fig. 5b, gas phase). Monomer **6** exhibited an identical absorbance shape to that of **1** with a decreased molar extinction coefficient (ε = 7.6 × 10^4 M^{-1} cm^{-1} at 360 nm) in comparison with that of **1**. Concentration-dependent absorbance showed that the intensity maintained a linear relationship and no new peaks were observed, suggesting that no aggregates or exciplex were formed at higher concentrations for either **1** or **6** (Fig. S4†). Meanwhile, the fluorescence spectra of **1** and **6** were almost the same, with two shoulder emissions at 474 and 504 nm and a tailing peak at around 537 nm (Fig. S5†). Moreover, similar fluorescence decay profiles for **1** and **6** were also observed with 15–16 ns fluorescent lifetimes (Fig. S5†). The similar optical properties of dimer **1** and monomer **6** indicate that a minimum conjugated structure formed between the two monomers after dimerization due to

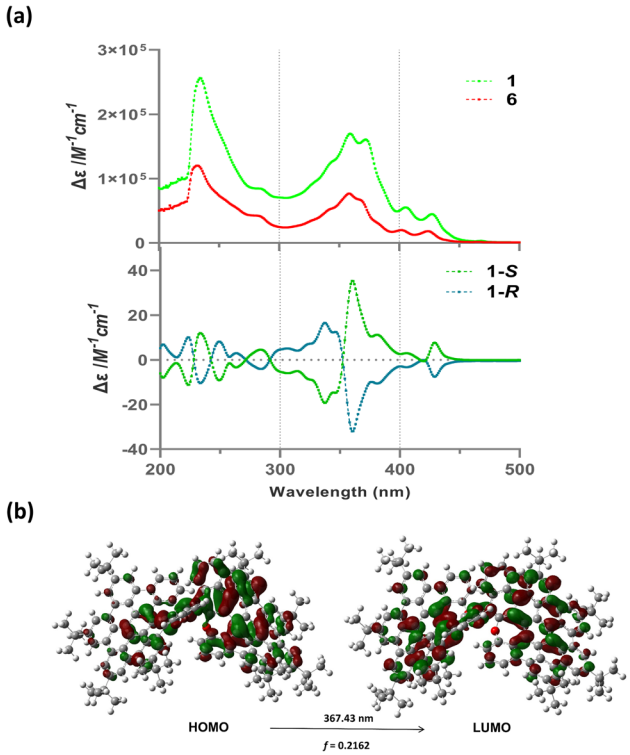

Fig. 5 (a) (Top) UV/vis absorption of **1** (green line) and **6** (red line). (Bottom) ECD spectra of **1**-*S* (green line) and **1**-*R* (cyan line). (b) TD-DFT calculated HOMO and LUMO orbitals and information of the TD-DFT calculated energy transition.

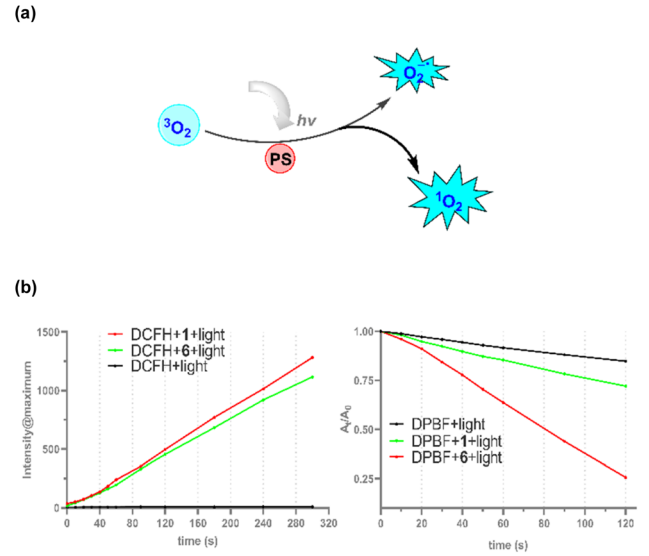

Fig. 6 ROS or singlet oxygen generation by using oxa-nanographenes **1** and **6** as photosensitizers. (a) Schematic illustration of the generation of reactive oxygen species (ROS) or singlet oxygen by the photosensitizing process. (b) Time-dependent fluorescence changes of the fluorescence probe DCFH upon white-light irradiation coexisting with NGs **1** and **6** (left). And normalized absorbance of DPBF (50 μM) at 411 nm in the presence of compound **1** (25 μM) or **6** (25 μM) upon white-light irradiation as a function of irradiation time (right).

the perpendicular conformation of atropisomerism. The specific optical rotation for (−)-1 and (+)-1 was found to be $[\alpha]25\ D = -270$ and +280 (1.0 mg mL^{-1} at 25 °C, Fig. S2†) and their electronic circular dichroism (CD) spectra demonstrated a perfect mirror-image relationship with multiple opposite Cotton effects in the UV/vis region from 200 to 450 nm, which confirmed their enantiomeric nature (Fig. 5a). In comparison with the simulated CD spectra calculated by time-dependent DFT (Fig. S20†), the two enantiomers could thus be assigned and the *R* enantiomer displayed a negative optical rotation. However, monomer **6**, with a [4]helicence unit, exhibited no sign to be separated by a chiral column due to a low enantiomerization barrier, suggesting that the chiroptical properties come from axial chirality. The CPL of the pair of atropisomers displayed opposite signals as expected (Fig. S5c†), with a dissymmetric factor of $|gCPL| = 2.4 \times 10^{-4}$ at 480 nm. The electrochemical properties of oxa-NG **1** and monomer **6** were investigated. The cyclic voltammetry revealed that oxa-NG **1** has two redox waves at 0.80/−0.10 and −0.73/−0.85 (Fig. S8†).

Oxa-nanographenes as a photosensitizer

Due to its large size and high molar extinction coefficient compared with that of biaryl derivatives, we tested if these oxa-NGs **1** could be used as an organic photosensitizer to transfer light energy into reactive oxygen species (ROS) or singlet oxygen (Fig. 6a) for potential application in photodynamic therapy (PDT).[24] The capacity of the ROS production of compound **1** was evaluated by 2′,7′-Dichlorofluorescein (DCFH), which emits green fluorescence with a 488 nm excitation after ROS oxidation, mainly $^1O_2$. Upon white-light irradiation for 300 s, a significantly brilliant DCFH green fluorescence at 540 nm was observed in the normoxic environment. And compound **6** can generate a slightly lower level of ROS in identical conditions. By contrast, the DCFH probe did not generate obvious emissions (Fig. 6b and S6†). Moreover, the ROS generation ability of oxa-NG **1** was further evidenced using 1,3-diphenylisobenzofuran (DPBF), a $^1O_2$ indicator. As indicated by the DPBF decay curves (Fig. 6b and S7†), irradiation of NG **1** with white light led to a sharp 75% decline, which is a significantly higher level than that of compound **6**. Collectively, oxa-NG **1** proved to be an effective photosensitizer to produce $^1O_2$-dominated ROS.

Conclusions

In summary, by referring to the axial chirality of BINOL, a novel BINOL-embedded atropisomeric chiral oxa-nanographene **1** was obtained by the selective dimerization of azopine-containing, HBC-like aromatics. The axial chirality of the new hydrocarbon was unambiguously confirmed by X-ray crystallography analysis of the crystallized enantiomers. The enantiomers were resolved and purified by chiral HPLC. The chiroptical properties, including CD, optical rotation, and CPL, were measured for each enantiomer and displayed opposite signals, as expected. Interestingly, the similar optical properties of the monomer and dimer indicate that the axially chiral conformation derived from the aryl–aryl single bond maintained the conformation of the monomer unit and minimum conjugated with each other. Furthermore, oxa-nanographene **1** was suggested as an efficient photosensitizer to transfer light energy to reactive oxygen species, mainly singlet oxygen.

Data availability

Detailed experimental procedures and analytical data are provided as the ESI.†

Author contributions

S. Li performed the major synthesis work and properties study. R. Li and B. Ma performed some synthetic work and spectra measurements. S. Wang performed the DFT calculations. Y.-K. Zhang performed the ROS and singlet oxygen generation test. B. Zhang and Y.-K. Zhang assisted with the NMR and spectra measurements. P. An conceived the concept and prepared the manuscript. All the authors analysed and interpreted the results.

Conflicts of interest

There are no conflicts of interest to declare.

Acknowledgements

We are grateful for the financial support provided by the National Natural Science Foundation of China (21901226 and 22061046). We thank the advanced analysis and measurement

centre of Yunnan University for assistance with instrumentation. Particularly, we thank Dr Jie Zhou for the X-ray analysis.

Notes and references

1 (*a*) M. Rickhaus, M. Mayor and M. Juríček, *Chem. Soc. Rev.*, 2017, **46**, 1643–1660; (*b*) S. H. Pun and Q. Miao, *Acc. Chem. Res.*, 2018, **51**, 1630–1642; (*c*) Y. Segawa, H. Ito and K. Itami, *Nat. Rev. Mater.*, 2016, **1**, 15002; (*d*) M. A. Majewski and M. Stępień, *Angew. Chem., Int. Ed.*, 2019, **58**, 86–116; (*e*) I. R. Márquez, S. Castro-Fernández, A. Millán and A. G. Campaña, *Chem. Commun.*, 2018, **54**, 6705–6718; (*f*) T. Kawase and H. Kurata, *Chem. Rev.*, 2006, **106**, 5250–5273; (*g*) Y.-T. Wu and J. S. Siegel, *Chem. Rev.*, 2006, **106**, 4843–4867; (*h*) R. A. Pascal, *Chem. Rev.*, 2006, **106**, 4809–4819; (*i*) X.-Y. Wang, X. Yao, A. Narita and K. Müllen, *Acc. Chem. Res.*, 2019, **52**, 2491–2505; (*j*) M. Hirai, N. Tanaka, M. Sakai and S. Yamaguchi, *Chem. Rev.*, 2019, **119**, 8291–8331; (*k*) M. Stępień, E. Gońka, M. Żyła and N. Sprutta, *Chem. Rev.*, 2017, **117**, 3479–3716; (*l*) A. Bedi and O. Godron, *Acc. Chem. Res.*, 2019, **52**, 2482–2490; (*m*) M. C. Stuparu, *Acc. Chem. Res.*, 2021, **54**, 2858–2870; (*n*) J. Wang, X. Zhang, H. Jia, S. Wang and P. Du, *Acc. Chem. Res.*, 2021, **54**, 4178–4190.

2 (*a*) J. M. Fernández-García, P. J. Evans, S. Filippone, M. Á. Herranz and N. Martín, *Acc. Chem. Res.*, 2019, **52**, 1565–1574; (*b*) S. Nishitani, R. Sekiya and T. Haino, *Angew. Chem., Int. Ed.*, 2020, **59**, 669–673; (*c*) M. Liu, L. Zhang and T. Wang, *Chem. Rev.*, 2015, **115**, 7304–7397; (*d*) T. Guo, A. Li, J. Xu, K. K. Baldridge and J. Siegel, *Angew. Chem., Int. Ed.*, 2021, **60**, 25809–25814; (*e*) J. M. Fernández-García, P. Izquierdo-García, M. Buendía, S. Filippone and N. Martín, *Chem. Commun.*, 2022, **58**, 2634–2645.

3 (*a*) V. Berezhnaia, M. Roy, N. Vanthuyne, M. Villa, J.-V. Naubron, J. Rodriguez, Y. Coquerel and M. Grngras, *J. Am. Chem. Soc.*, 2017, **139**, 18508–18511; (*b*) C. Shen, G. Zhang, Y. Ding, N. Yang, F. Gan, J. Vrassous and H. Qiu, *Nat. Commun.*, 2021, **12**, 2867; (*c*) Y. Liu, Z. Ma, Z. Wang and W. Jiang, *J. Am. Chem. Soc.*, 2022, **144**, 11397–11404; (*d*) C. Duan, J. Zhang, J. Xiang, X. Yang and X. Cao, *Angew. Chem., Int. Ed.*, 2022, **61**, e202201494; (*e*) Y.-F. Wu, S.-W. Ying, S.-D. Liao, L. Zhang, J.-J. Du, B.-W. Chen, H.-R. Tian, F.-F. Xie, H. Xu, S.-L. Deng, Q. Zhang, S.-Y. Xie and L.-S. Zheng, *Angew. Chem., Int. Ed.*, 2022, **61**, e202204334.

4 (*a*) Y. Hu, X.-Y. Wang, P.-X. Peng, X.-C. Wang, X.-Y. Cao, X. Feng, K. Müllen and A. Narita, *Angew. Chem., Int. Ed.*, 2017, **56**, 3374–3378; (*b*) K. Kato, Y. Segawa, L. T. Scott and K. Itami, *Angew. Chem., Int. Ed.*, 2018, **57**, 1337–1341; (*c*) S. Suárez-Pantiga, P. Redero, X. Aniban, M. Simon, C. Golz, R. A. Mata and M. Alcarazo, *Chem.–Eur. J.*, 2021, **27**, 13358–13366; (*d*) Y. Nakakuki, T. Hirose, H. Sotome, H. Miyasaka and K. Matsuda, *J. Am. Chem. Soc.*, 2018, **140**, 4317–4326; (*e*) Z. Qiu, C.-W. Ju, L. Frédéric, Y. Hu, D. Schollmeyer, G. Pieters, K. Müllen and A. Narita, *J. Am. Chem. Soc.*, 2021, **143**, 4661–4667; (*f*) H. Marom, S. Pogodin and I. Agranat, *Polycyclic Aromat. Compd.*, 2007, **27**, 295–310; (*g*) J. Wang, C. Shen, G. Zhang, F. Gan, Y. Ding and H. Qiu, *Angew. Chem., Int. Ed.*, 2022, **61**, e20211597.

5 (*a*) Z. Qiu, S. Asako, Y. Hu, C.-W. Ju, T. Liu, L. Rondin, D. Schollmeyer, J.-S. Lauret, K. Müllen and A. Narita, *J. Am. Chem. Soc.*, 2020, **142**, 14814–14819; (*b*) P. An, R. Li, B. Ma, R.-Y. He, Y.-K. Zhang, M.-J. Xiao and B. Zhang, *Angew. Chem., Int. Ed.*, 2021, **60**, 24478–24483; (*c*) D. Reger, P. Haines, K. Y. Amsharov, J. A. Schmidt, T. Ullrich, S. Bönish, F. Hampel, A. Görling, J. Nelson, K. E. Jelfs, D. M. Guldi and N. Jux, *Angew. Chem., Int. Ed.*, 2021, **60**, 18073–18081; (*d*) R. Li, B. Ma, R.-Y. He, B. Zhang, Y.-K. Zhang, S.-Y. Feng and P. An, *Chem.–Asian J.*, 2022, **17**, e202101365; (*e*) C. Schaack, A. M. Evans, F. Ng, M. L. Steigerwald and C. Nuckolls, *J. Am. Chem. Soc.*, 2022, **144**, 42–51.

6 (*a*) J. Wu, W. Pisula and K. Müllen, *Chem. Rev.*, 2007, **107**, 718–747; (*b*) A. J. Berresheim, M. Müller and K. Müllen, *Chem. Rev.*, 1999, **99**, 1747–1785; (*c*) J. Wu, M. D. Watson, L. Zhang, Z. Wang and K. Müllen, *J. Am. Chem. Soc.*, 2004, **126**, 177–186; (*d*) M. Grzybowski, K. Skonieczny, H. Butenschön and D. T. Gryko, *Angew. Chem., Int. Ed.*, 2013, **52**, 9900–9930; (*e*) K. Müllen and J. P. Rabe, *Acc. Chem. Res.*, 2008, **41**, 511–520.

7 (*a*) H. Arslan, F. J. Uribe-Romo, B. J. Smith and W. R. Dichtel, *Chem. Sci.*, 2013, **4**, 3973–3978; (*b*) L. Barnett, D. M. Ho, K. K. Baldridge and R. A. Pascal Jr, *J. Am. Chem. Soc.*, 1999, **121**, 727–733; (*c*) M. A. Medel, R. Tapia, V. Blanco, D. Miguel, S. P. Morcillo and A. G. Campaña, *Angew. Chem., Int. Ed.*, 2021, **60**, 6094–6100; (*d*) M. A. Medel, C. M. Cruz, D. Miguel, V. Blanco, S. P. Morcillo and A. G. Campaña, *Angew. Chem., Int. Ed.*, 2021, **60**, 22051–22056.

8 (*a*) Y. Zhu, X. Guo, Y. Li and J. Wang, *J. Am. Chem. Soc.*, 2019, **141**, 5511–5517; (*b*) S. Ma, J. Gu, C. Lin, Z. Luo, Y. Zhu and J. Wang, *J. Am. Chem. Soc.*, 2020, **142**, 16887–16893; (*c*) C. M. Cruz, S. Castro-Fernández, E. Macôas, J. M. Cuerva and A. G. Campaña, *Angew. Chem., Int. Ed.*, 2018, **57**, 14782–14786.

9 D. Reger, P. Haines, F. W. Heinemann, D. M. Guldi and N. Jux, *Angew. Chem., Int. Ed.*, 2018, **57**, 5938–5942.

10 P. J. Evans, J. Ouyang, L. Favereau, J. Crassous, I. Fernández, M. A. Petrukhina, J. Perles and N. Martín, *Angew. Chem., Int. Ed.*, 2018, **57**, 6774–6779.

11 C. M. Cruz, I. R. Márquez, I. F. A. Mariz, V. Blanco, C. Sanchez-Sánchez, J. M. Sobrado, J. A. Martín-Gago, J. M. Cuerva, E. Maçôas and A. G. Campaña, *Chem. Sci.*, 2018, **9**, 3917–3924.

12 J. Ma, Y. Fu, E. Dmitrieva, F. Liu, H. Komber, F. Hennersdorf, A. A. Popov, J. J. Weigand, J. Liu and X. Feng, *Angew. Chem., Int. Ed.*, 2020, **59**, 5637–5642.

13 P. Izquierdo-García, J. M. Fernández, I. Fernández, J. Perles and N. Martín, *J. Am. Chem. Soc.*, 2021, **143**, 11864–11870.

14 (*a*) L. Pu, *Chem. Rev.*, 1998, **98**, 2405–2494; (*b*) J. M. Brunel, *Chem. Rev.*, 2005, **105**, 857–897.

15 (*a*) W. Yang, R. Bam, V. J. Catalano and W. A. Chalifoux, *Angew. Chem., Int. Ed.*, 2018, **57**, 14773–14777; (*b*) K. Hassan, K.-I. Yamashita, K. Hirabayashi, T. Shimizu,

K. Nakabayashi, Y. Imai, T. Matsumoto, A. Yamano and K.-I. Sugiura, *Chem. Lett.*, 2015, **44**, 1607–1609; (*c*) Y. Uchida, T. Hirose, T. Nakashima, T. Kawai and K. Matsuda, *Org. Lett.*, 2016, **18**, 2118–2121.

16 (*a*) K. Sato, M. Hasegawa, Y. Nojima, N. Hara, T. Nishiuchi, Y. Imai and Y. Mazaki, *Chem.–Eur. J.*, 2021, **27**, 1323–1329; (*b*) Y. Nojima, M. Hasegawa, N. Hara, Y. Imai and Y. Mazaki, *Chem. Commun.*, 2019, **55**, 2749–2752; (*c*) P. Fang, M. Chen, X. Zhang and P. Du, *Chem. Commun.*, 2022, **58**, 8278–8281.

17 G. Ouyang, J. Rühe, Y. Zhang, M.-J. Lin and F. Würthner, *Angew. Chem., Int. Ed.*, 2022, **61**, e202206706.

18 R. K. Dubey, M. Melle-Franco and A. Mateo-Alonso, *J. Am. Chem. Soc.*, 2022, **144**, 2765–2774.

19 (*a*) F. Toda, K. Tanaka and S. Iwata, *J. Org. Chem.*, 1989, **54**, 3007–3009; (*b*) D. Villemin and F. Sauvaget, *Synlett*, 1994, 435–436.

20 (*a*) T. Sakamoto, H. Yonehara and C. Pac, *J. Org. Chem.*, 1994, **59**, 6859–6861; (*b*) T. Sakamoto, H. Yonehara and C. Pac, *J. Org. Chem.*, 1997, **62**, 3194–3199.

21 Deposition Numbers 2193890 for compound **1**, contain the supplementary crystallographic data for this paper.

22 K. Mori, Y. Masuda and S. Kashino, *Acta Crystallogr., Sect. C: Cryst. Struct. Commun.*, 1993, **49**, 1224–1227.

23 L. Meca, D. Řeha and Z. Havlas, *J. Org. Chem.*, 2003, **68**, 5677–5680.

24 M. Lan, S. Zhao, W. Liu, C.-S. Lee, W. Zhang and P. Wang, *Adv. Healthcare Mater.*, 2019, **8**, 1900132.